Microscale intrinsic properties of hybrid unidirectional/woven composite laminates: Part Ⅰ experimental tests

Junjie Ye[a,b], Heng Cai[a], Lu Liu[a], Zhi Zhai[d], Amaechi Chiemela Victor[b], Yongkun Wang[a], Lei Wan[c], Dongmin Yang[c,*], Xuefeng Chen[d], Jianqiao Ye[b,*]

[a] Research Center for Applied Mechanics, Key Laboratory of Ministry of Education for Electronic Equipment Structure Design, Xidian University, Xi'an 710071, China

[b] Department of Engineering, Lancaster University, Lancaster LA1 4YW, UK

[c] Institute for Materials and Processes, School of Engineering, University of Edinburgh, EH9 3FB, Edinburgh, UK

[d] State Key Laboratory for Manufacturing Systems Engineering, Xi'an Jiaotong University, Xi'an 710049, China

Abstract

An insight understanding of failure of composites is critical for evaluating safety and reliability of the materials when they are in service. In this research, a combined image analysis technique using computed microtomography (micro-CT) and scanning electron microscopy (SEM) is proposed to study the microstructures, damage and failure of fibre-reinforced composites. The CT is used to extract the 3D microscale morphology and identify the internal failure behaviors of a hybrid unidirectional/woven composite laminate (HUWCL). A series of material parameters, such as fiber volume fraction, void ratio, layer mode, are acquired by the statistical analysis of the micro-CT images. In addition, microscale surface damage and failure mechanism of woven and unidirectional (UD) laminae are further investigated by SEM. It is found that the matrix damage around the interface always occurs in both the woven and the unidirectional (UD) laminae, and distinct delamination is found between the UD laminae and the woven composites. The study shows a great potential of combining micro-CT with SEM in revealing local damage and intrinsic failure mechanism in the HUWCL at microscale.

Keywords: Hybrid laminates; Micro-CT; Failure mechanism; Damage evolution; SEM.

1. Introduction

Due to the outstanding design flexibility and mechanical performance, laminated unidirectional and woven fiber-reinforced composites have been widely used in the lightweight structures for aircrafts, satellites and automobiles, etc. [1-4]. In service, composite laminates may be subjected to complex external loadings, which generates significant local stresses, resulting in microscale damages [5-7] and eventually causing a catastrophic structural failure. With the consideration of structural integrity and reliability of composite laminates, it is critical for designers to understand their failure mechanisms [8-10].

A large number of studies have contributed to the investigations of damage mechanisms and failure prediction of composite laminates layered up from unidirectional (UD) laminae using experimental tests as well as theoretical methods [11-12]. Zhang et al., [13] employed a three-dimensional (3D) model to study the progressive damage mechanisms of open-hole composite laminates subjected to a longitudinal load with consideration of fiber kinking and shear non-linearity. The numerical results

*Corresponding authors.
Email address: Dongmin.Yang@ed.ac.uk (Dongmin Yang); j.ye2@lancaster.ac.uk (Jianqiao Ye)

indicated that the damage in the 0° UD laminae could be used as an indicator to reflect the damage level of composite laminates. At microscale, Parambil and Gururaja [14] studied the damage mechanisms (matrix damage, fiber failure and fiber-matrix interface debonding) of composite laminates with random micro-structures. It was revealed that interfacial debonding and matrix damage played a dominant role in determining the average responses of composites under transverse loads and combined transverse and shear loading conditions. The studies mentioned above were restricted to microscale damage initiation and evolutions in composites. More comprehensive studies regarding multi-scale modelling were carried out in Refs. [15-17] to understand failure mechanisms of composites from microscale damage to macroscopic fracture, thus, to optimize the microstructure [18]. Ye et al., [19] proposed a multi-scale model based on a generalized method of cells (GMC) to investigate the damage evolution paths of open-hole composite laminates. The results showed tha the cracks firstly appeared in the 90° laminae and accumulated along the thickness direction. However, the aforementioned studies are limited to the failure analysis of composite laminates under uniaxial loads. Boddeti et al., [20] developed a multiscale topological optimization method for optimal design and fabrication of composite laminates. The capability of the proposed method was verified by experiments. Traditionally, due to the limitations of experimental techniques, surface cracks or damages are captured by experiments, while the internal damage evolutions are mostly predicted by numerical simulations. To clearly visualize internal damage and voids of a material, X-ray computed microtomography (micro-CT) technology was introduced in recent years. Qiao et al., [21] studied the multi-axial fatigue failures of notched composite laminates and the effects of notch configuration using micro-CT images. The results shown that the damage evolution under fatigue loading was substantially different compared to that under a quasi-static loading. Nguyen et al., [22] analyzed in-plane and out-of-plane fiber misalignment in carbon fiber reinforced laminates by employing micro-CT techniques. The results can be useful for the determination of fiber orientation in composites for, e.g., vacuum assisted resin transfer moulding and autoclave manufacturing.

Composite laminates made by a series of UD laminae are vulnerable under impact loading [29] and drilling [23-24], since the loads can induce fiber fractures, matrix cracking and delamination within the composites. Compared with the UD laminae, the velocity of longitudinal strain wave in the woven composites decreases due to the crimped reinforced fibers, which are helpful for energy absorption. To mitigate local damage in composite laminates and improve their service life, hybrid composite laminates, composed of outer woven and inner unidirectional plies, have been designed and used in A220 passenger aircraft wings [24]. Liu et al., [24-25] carried out experimental and numerical studies on crash behaviors and compression-after-impact strength of hybrid unidirectional/woven composite laminate (HUWCL). The proposed numerical method could significantly reduce the amount of physical tests required in the development of crashworthy structures. Moleiro et al., [26] proposed a mixed model to analyze the coupled hygro-thermo-mechanical behaviors of hybrid fiber laminates and sandwich plates. The model was verified and is capable of accurately predicting the stresses, heat flux and moisture flux in the thickness direction. Gupta and Ghosh [27] investigated the dynamic properties of the HUWCL based on the nonpolynomial shear deformation theory. Mahmoud et al., [28] focused on experimental and theoretical analysis of damage mechanisms of HUWCL under impact loading. A semi-continuous strategy for the modelling of impacts on the HUWCL was validated by the experimental results. It is clear from the aforementioned research, HUWCL at microscale and the initial micro-voids were

not considered.

This paper aims to propose a combined imaging technique using both micro-CT and SEM to investigate the failure of HUWCL. The techniques can be extended to study other composites. The outline of this paper is as follows. Microscale morphology of the HUWCL is obtained by X-ray micro-CT, and the key material parameters, including fiber orientation in woven, layer thickness and internal voids, are determined in Section 2. In section 3, mechanical tests are conducted on the HUWCL to acquire its stress-strain properties and elastic modulus. In Section 4, the delamination between the woven composites and UD laminae, as well as the internal damage in the UD are discussed based on the 3D micro-CT images. In section 5, SEM is further employed to observe the interfacial properties between fibers and matrix within the UD laminae and the woven layer. Conclusions are finally drawn in Section 6.

2. Microscale morphology of the HUWCL

Micro-CT has been one of the most effective non-destructive techniques to provide three-dimensional images of material structure and internal damage at microscale and sub-microscale levels [29-30]. To accurately capture the microscale morphology and microstructural parameters of the HUWCL, micro-CT analysis of the specimen (EXTREN) was executed on a Zeiss Xradia Versa 410 micro-CT system. During the characterization process, the scanned specimen was placed on a rotating stage, and 1800 2D X-ray projections were acquired spanning 360° of tomographic rotation at an increment of 0.2°. A spatial resolution of 6.8 μm was achieved in the selected region of interest. An accelerating voltage of 80 kV and a power of 7 W for the X-ray source were used for better imaging quality. The total scan time was about 4h for each specimen. The raw 2D projections were reconstructed using a Zeiss built-in reconstruction software to obtain full 3D scanned images, which were then visualized and analyzed using Avizo software.

2.1. Layer structure of the HUWCL

In order to identify the microscale morphology of the constituent materials, the watershed algorithm proposed by Mangan [31] was employed. Fig. 1(a) is a 3D image of the intact specimen obtained by micro-CT. Here, the fiber orientation of the laminae along the x_1-aixs was defined as the longitudinal direction for the HUWCL. Naturally, the fiber orientation of the laminae along the x_3-aixs was defined as the transverse direction in the global coordinate system. Due to the symmetry of the HUWCL, a part of local microscale structure was portioned for a better view, as shown in Fig. 1(b).

To identify the microscale structures of the HUWCL, e.g., layer thickness, void ratio, a tomographic image across F-F plan acquired by Avizo software in Fig. 1(a) is shown in Fig. 2. It can be found that the HUWCL has an approximate thickness of 3.256 mm, and consists of two layers of 0° UD laminae and three layers of woven composites. In addition, it should be noted that the first layer contains six plies of woven laminae. The void ratio of the woven laminae is approximate to 0.5%, which is lower than the void ratio of the UD laminae (1.2%). The thickness and fiber volume fraction (FVF) of each layer can be found in Table 1. Specifically, the second and fourth layers are 0° UD laminae, the thickness of which are 355 μm and 627 μm, respectively. However, it is hard to identify the number of plies in the UD laminae. According to the statistical results of the micro-CT scans, the FVF of these two UD laminae are approximately 21.9%. The thickness of the first, the third and the fifth woven layers are 978 μm, 318 μm and 978 μm, respectively. Their fiber volume fractions are

all approximately 17.8%.

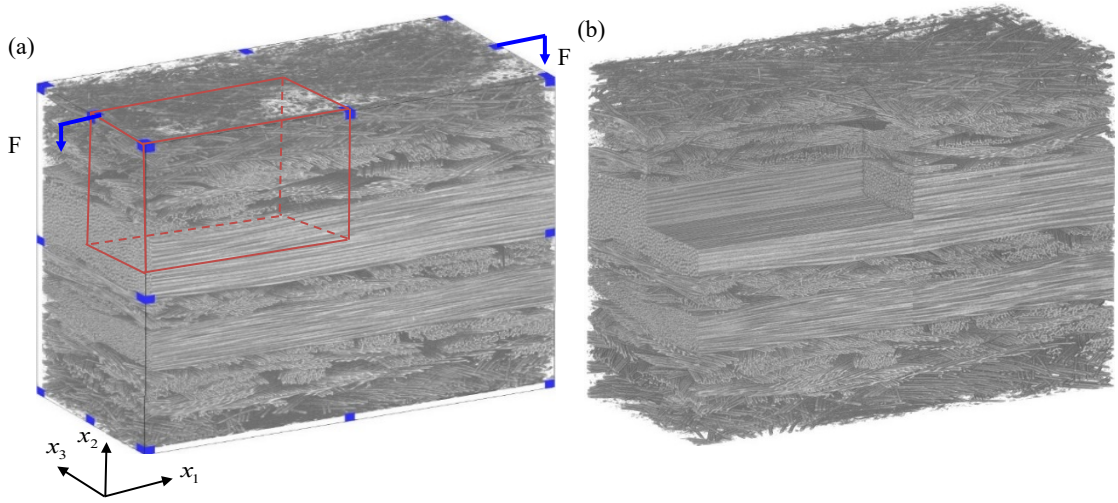

Fig. 1. Micro-CT image of HUWCLs: (a) Full view, and (b) Partitioned view

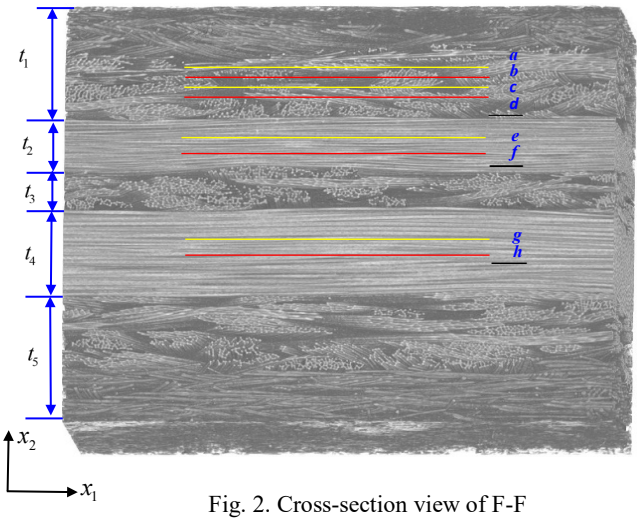

Fig. 2. Cross-section view of F-F

Table 1. Microstructural details of the HUWCL

Layer number	Type	Number of plies	Thickness/μm	Fiber volume fraction	Void ratio
1st layer	Woven laminae	6	t_1=978	17.8%	0.4%
2nd layer	UD laminae	N/A	t_2=355	21.9%	1.2%
3rdlayer	Woven laminae	2	t_3=318	17.8%	0.5%
4th layer	UD laminae	N/A	t_4=627	21.9%	1.0%
5th layer	Woven laminae	6	t_5=978	17.8%	0.3%

2.2. Fiber distributions in the woven and the UD layers

To explore fiber distribution in the UD laminae and fiber undulation in the woven layer, 3D images generated by Avizo software are shown, respectively, in Fig. 3(a) and Fig. 3(c). To further observe their microscale morphology and fiber distributions, zoomed-in images are shown in Fig. 3(b) and Fig. 3(d), respectively, where matrix materials around the fibers are made transparent to provide a clearer view of the fibers. It can be found from the cross-section image of the UD lamina, as shown

in Fig. 3(b), that the circular fibers are periodically distributed approximately in the matrix materials. Figs. 3 (e)-(g) are the profile images along the axes of H-H', J-J' and K-K' (Fig. 3(d)), respectively. The fiber undulation in the woven layers can be determined from these profile images. The black dots shown in Fig. 4 are the geometric center of the undulation fibers, which takes the average position of the individual fibers. The solid lines are the fitting curves measured from the microscale images to effectively determine the actual fiber orientations.

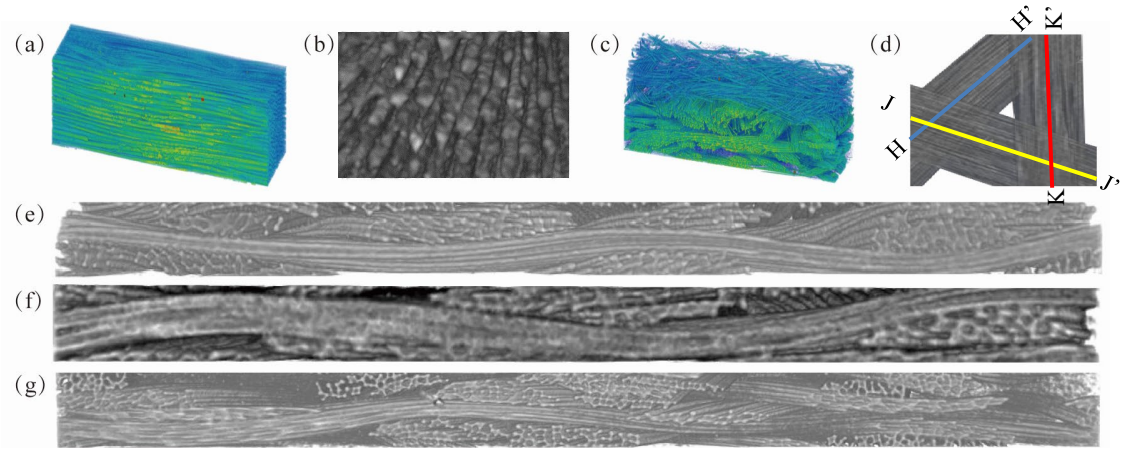

Fig. 3. Microscopic morphology of the HUWCL (a) 3D image of the UD lamina (b) zoom-in image of the UD lamina (c) 3D image of the woven layer (d) zoom-in image of the woven composites (e) H-H' profile image (f) J-J' profile image (g) K-K' profile image

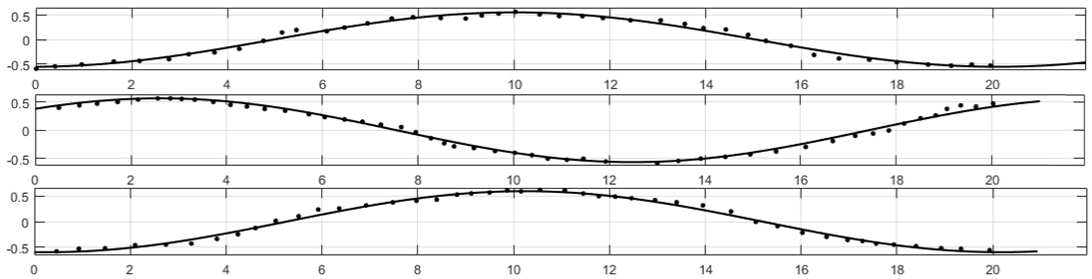

Fig. 4. Fiber undulation in the woven layer (dmm)

2.3. Statistics of the void ratio

Initial voids in composites are inevitably produced during the manufacturing process. As one of the image segmentation technologies whose principle is to divide image pixel points into several categories, the watershed algorithm [31], was employed to distinguish material constituents and initial voids. During the image reconstruction stage, the threshold of fibers can be easily determined to be 14 μm according to their diameters. In addition, the initial voids were identified due to their high differentiation degrees compared with reinforcing fibers or matrix materials. After determining the initial voids and reinforcing fibers, the rest of material constituent are considered to be matrix materials.

Fig. 5 shows the images of the slices extracted from the sub-layer of the woven laminae along the thickness direction (x_2-axis). The corresponding locations of the four slices (located at x_1-x_3 plane)

are numbered as ‘a’ to ‘d’, as shown in Fig. 2, and the vertical distance between any two adjacent slices is 80 μm. From the images shown in Fig. 5(a)-(b), a few initial voids marked with red boxes in the braided layer can be found. To easily observe these defects, the zoom-in graphs marked with dashed red boxes are also provided. It can be seen that these elliptical or nearly circular voids are mostly distributed in the vicinity of fiber surfaces, which is likely attributed to insufficient wetting-out during the manufacturing process. Similar manufacturing induced damages are found as shown in Figs. 5(c)-(d). According to the statistic results of the void volume derived from the 3D micro-CT images, the void ratio in the first, third and fifth woven layers are approximately 0.4%, 0.5% and 0.3%, respectively. However, it should be noted that voids are rarely noticeable in the locations far away from the fabric fibers.

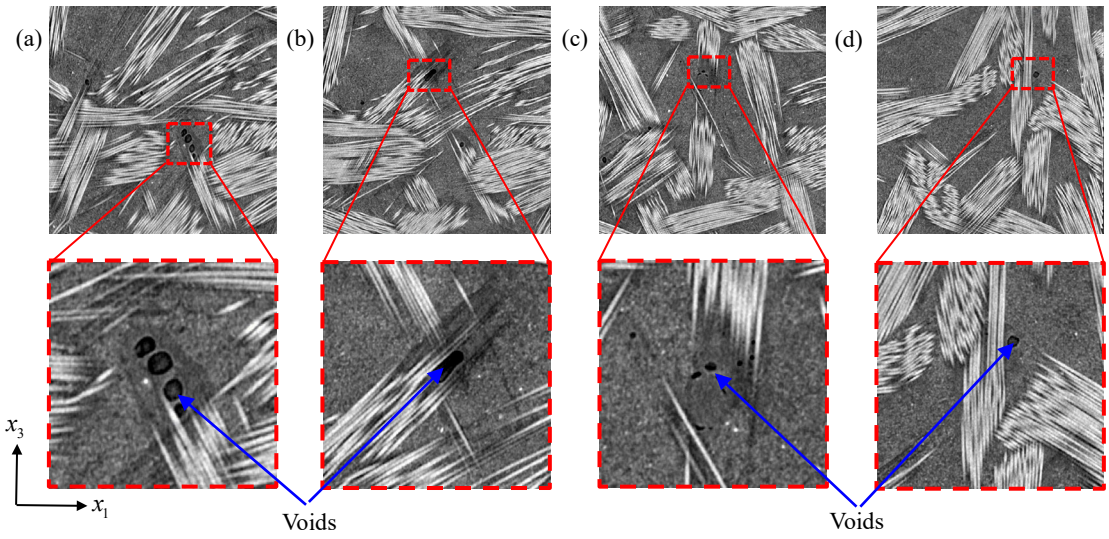

Fig. 5. Sliced images extracted from the woven layers along the thickness direction

To explore the void distributions in the UD laminae, four slices extracted from the second and the fourth layers along the thickness direction (x_2 axis) are shown in Fig. 6. The corresponding locations of the four slices (located at x_1-x_3 plane) are numbered as ‘e’ to ‘h’ as shown in Fig. 2. In general, the appearance of internal voids/defects located in the UD laminae is distinctively different to those in the woven layers due to their different geometrical characteristics. From Fig. 6(a)-(b), some elliptical voids, distributed in the matrix among fibers, can be easily detected, which are mainly in parallel to the fiber direction. Voids of similar shape, which could significantly reduce loading transfer between fibers and matrix, can also be found in Fig.6(c)-(d). In addition, the void ratio in the UD laminae tends to be sharply increased according to the statistical results compared to the woven layer. In details, the void ratios of the second and the fourth UD laminae are approximately 1.2% and 1.0%, respectively.

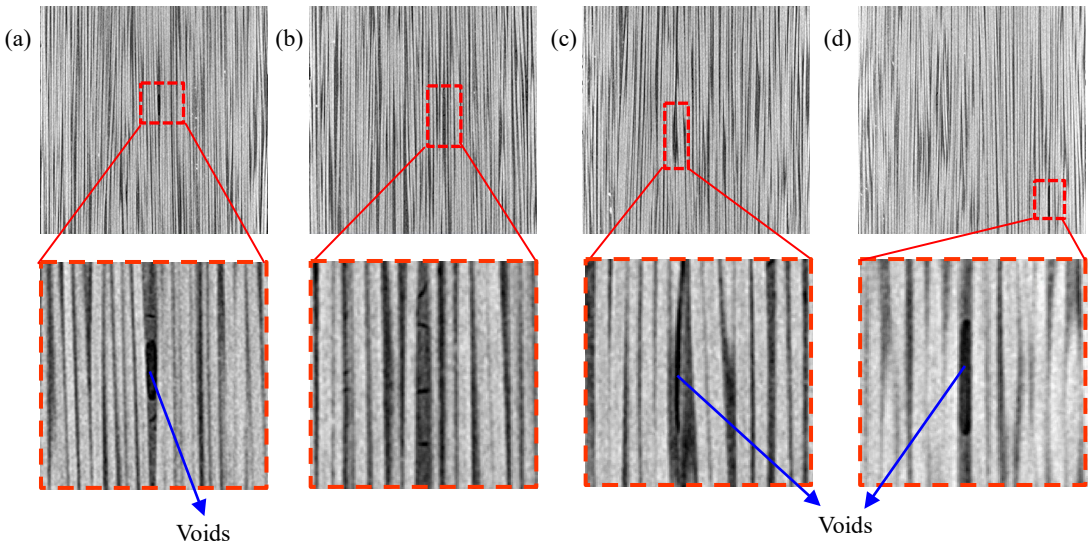

Fig. 6. Sliced images extracted from the UD laminae along the thickness direction

3. Mechanical tests on the HUWCL

3.1. Stress-strain properties under tensile load

To acquire mechanical properties of the HUWCL, uniaxial tensile loadings along the x_1-axis and the x_3-axis are, respectively, applied on the specimens. The length and width of the specimen are, respectively, 250mm and 25mm according to the standard of ASTM D3039/D 3039M-00. The Material Test System (MTS, Instron 8802J5219, 250NK, Norwood, MA, USA) shown in Fig. 7(a) is used to impose a constant strain rate of 5×10^{-5} on the specimens under the room temperature. Figs. 7(b)-(c) show the fixture and the fractured specimen, respectively.

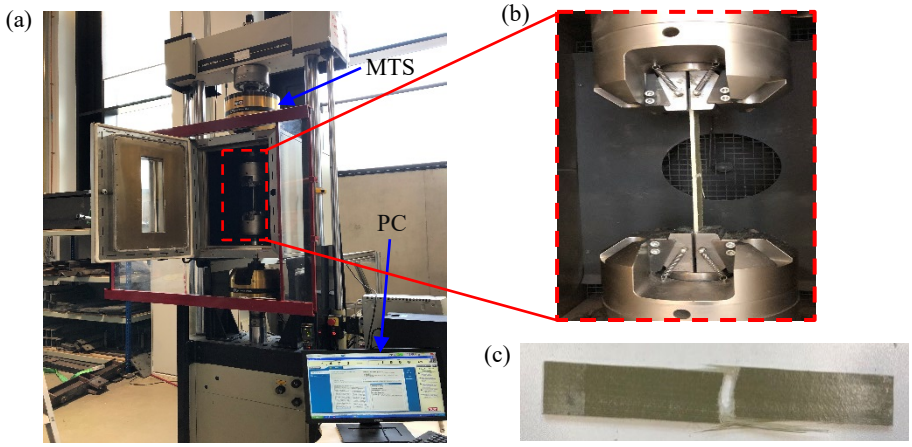

Fig. 7. Experimental tests of the HUWCL (a) Test system (b) Fixture (c) Fractured specimen

Fig. 8(a) presents the stress-strain curves of the three 0° specimens obtained from the experiments. The stresses are calculated by dividing the applied forces by the specimen's original cross-sections. The stress-strain curves agree with each other well, and the average failure strength is approximately 252.4MPa. For comparisons, the same test procedure is followed to test the three 90° specimens, and the experimental results are shown in Fig. 8(b). The stiffness and the failure strength are much lower in the 90° specimens, and the average failure strength is approximately 84.3MPa. The reduction in the stiffness and the failure strength is attributed to the fiber architecture

shown in Fig. 2, where the uniaxial fibers are in the 0° direction. In addition, unlike the 0° UD laminae, which present a linear stress-strain response under the longitudinal tension, both the 0° and the 90° HUWCL demonstrate noticeable nonlinear behaviors due to the combined effect of matrix plastic deformation and the fiber undulation in the woven layer.

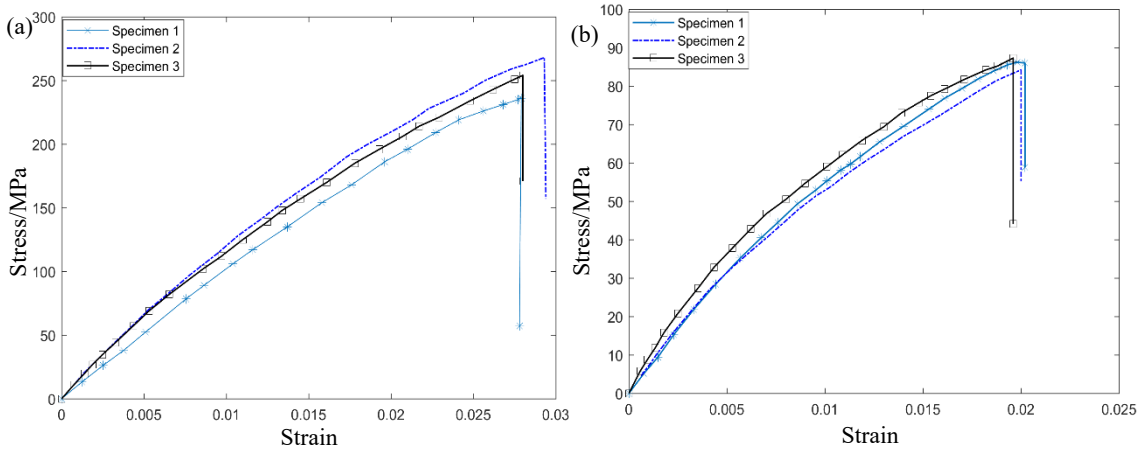

Fig. 8. Test results of the HUWCL under uniaxial tensile loading (a) HUWCL with $0°$ continuous fiber composites (b) HUWCL with $90°$ continuous fiber composites

3.2. Elastic modulus

At the initial stage, a linear proportional relationship between the total strain and the average stress is observed as shown in Fig. 8. According to the standard test methods for Young's modulus shown in the test standard of ASTM E111-17, the longitudinal and transversal moduli can be obtained by the ratio of the tensile stress increment $\Delta\sigma_i$ to the corresponding strain increment $\Delta\varepsilon_i$, that is,

$$E_i = \frac{\Delta\sigma_i}{\Delta\varepsilon_i} \qquad (i = 1, 3) \tag{1}$$

where the subscripts $i = 1$, 3 denote the loading directions, i.e., along either the x_1- or the x_3-directions, as shown in Fig. 1(a). Here, it should be pointed out that the applied maximum stress for determining the effective modulus should be lower than the proportional limit of the material. Table 2 present the experimental results of the effective modulus. It can be seen that the average moduli of the HUWCL in the longitudinal and transversal directions are 12.1Gpa, and 7.3Gpa, respectively.

Table 2. Comparisons of tensile moduli for the HUWCL

Methods	Specimen number	$0°$ HUWCL/GPa	$90°$ HUWCL/GPa
Experimental tests	Specimen 1	13.2	8.2
	Specimen 2	12.8	7.1
	Specimen 3	10.4	6.6
Average values		12.1	7.3

4. Internal damage morphology and failure mechanisms

4.1. Microscale damage in the HUWCL

To further study the microscale damage mechanisms of the HUWCL, 3D images of the fractured specimen are shown in Fig. 9, which was obtained by micro-CT imaging. Fig. 9(a) shows that the main failure modes of the woven layers are fiber pullouts and breakages. Fig. 9(b) is a side view of

the HUWCL to show the damage modes in the UD laminae. Matrix cracks are found in the UD laminae due to the transverse loading, resulting in transverse matrix cracking that is the main damage mode. In addition, delamination between the woven layer and the UD laminae is clearly seen. However, it is interesting to mention that no obvious delamination occurs between the sub-plies of the woven layers.

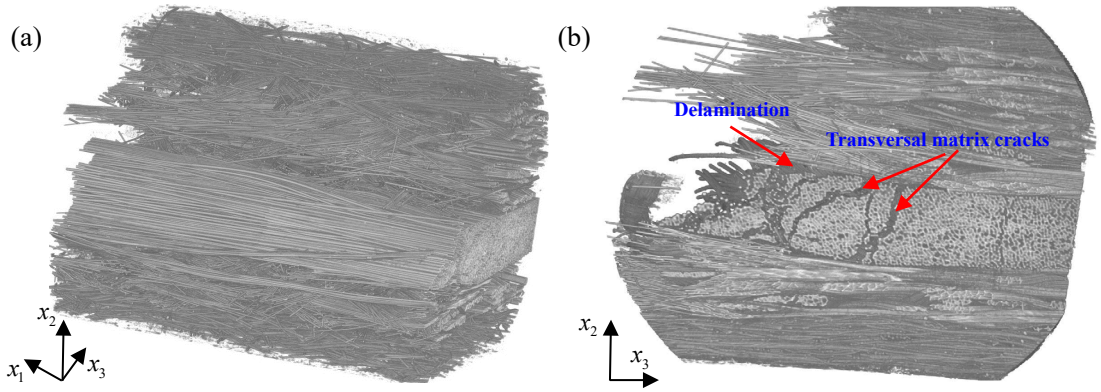

Fig. 9. Microscopic morphology of the fractured specimen: (a) Fractured surface (b) Side view

To better capture the interlaminar failures in the HUWCL, three-dimensional morphology of the fractured specimen was further rended by the colormap (see Fig. 10(a)). It should be pointed out that the thresholds of fibers changed according to the attenuation degree of X-ray penetrating the specimen. Silce interval of 874 μm along x_1 axis was considered, and the four images were acquired according to the slice locations labelled as '*i*' to '*l*', as shown in Fig.10(b)-(e). It can be seen from the figure that delaminations indicated by the red lines are located at the interfaces between the UD laminae and the woven layer. These delamination damage may be attributed to the mismatch of the effective moduli between the woven layers and the UD laminae, which leads to an uneven stress distribution and stress concentration at the interlaminar interface. From the comparisons between Fig. 10(c) and Fig. 10(e), a strong correlation between the interlaminar delamination and the matrix cracking in the UD laminae can be easily found.

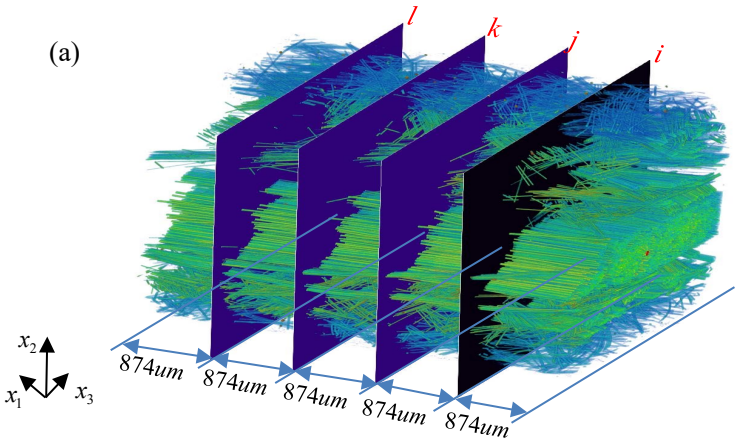

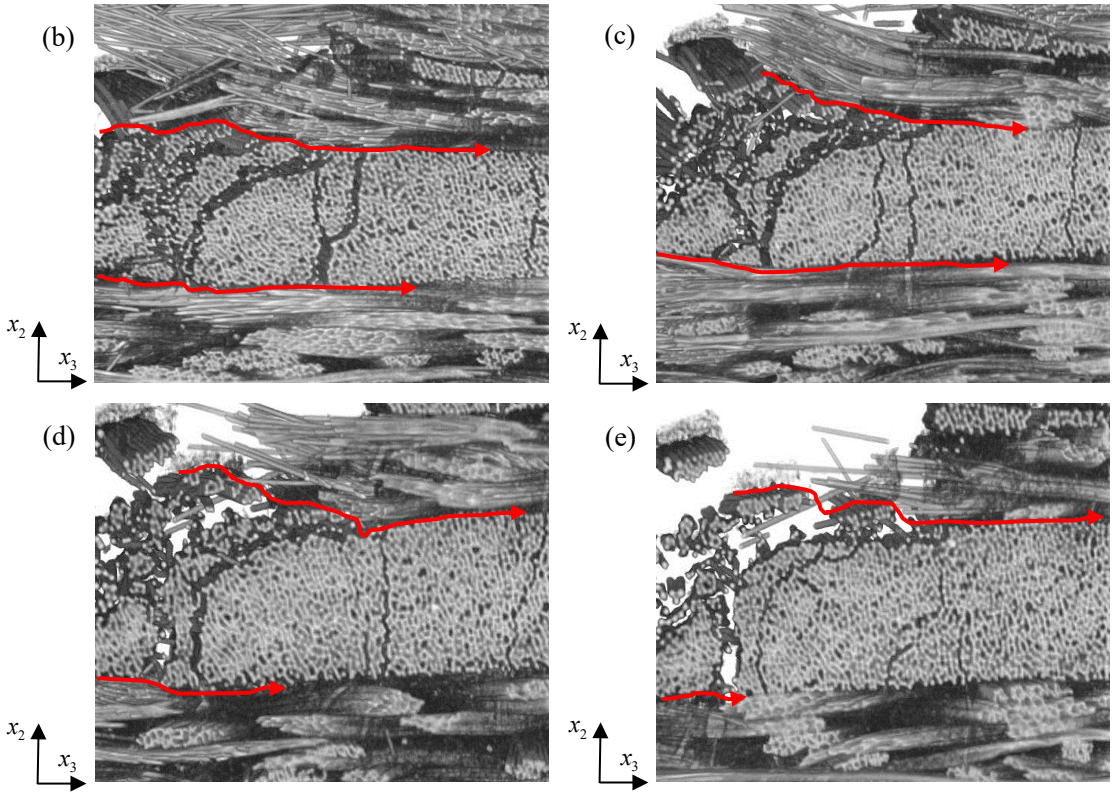

Fig. 10. Slices of microscopic morphology along x_1-direction: (a) CT colourmap of the fractured region, (b) Cross-section *i,* (c) Cross-section *j,* (d) Cross-section *k,* and (e) Cross-section *l.*

4.2. Microscale damage in the UD lamina

Fig. 11 focuses on the internal damage in the UD laminae. Fig. 11(a) presents the 3D microstructure of the UD composite laminae, including the internal damage in the matrix. The 3D microstructure of the UD laminae is extracted from a damaged region of the HUWCL, which is marked by a black rectangular box in Fig. 11(a). In order to better visualize the internal damage in the UD laminae, the extracted UD laminae are further divided into the two slices along the thickness direction, as illustrated in Fig. 11(b)-(c). It should be noted that the blue, green and yellow fields denote the air, the matrix and the fibers in Fig. 11(d), respectively. The matrix (as coloured in green) was filtered from the visualization as much as possible. However, due to the approximate thresholds between fibers and matrix in the image process of Avizo software, some transitional colours, such as light orange, can be found in the figure. The transverse matrix cracks inside the UD laminae are marked with blue color (the same as the color for air). However, it is noted that the occurrence of the light orange zone has little effect on the identification of microscale damage. Combing with Fig. 10, it can be concluded that the extension of transverse damage cracks was highly dependent on the distribution of internal defects and the edge effects. Most of the transverse cracks started from the edge of the specimen. The cracks prorogated to the interior in the matrix along the fiber direction, with a decreasing width from the edge.

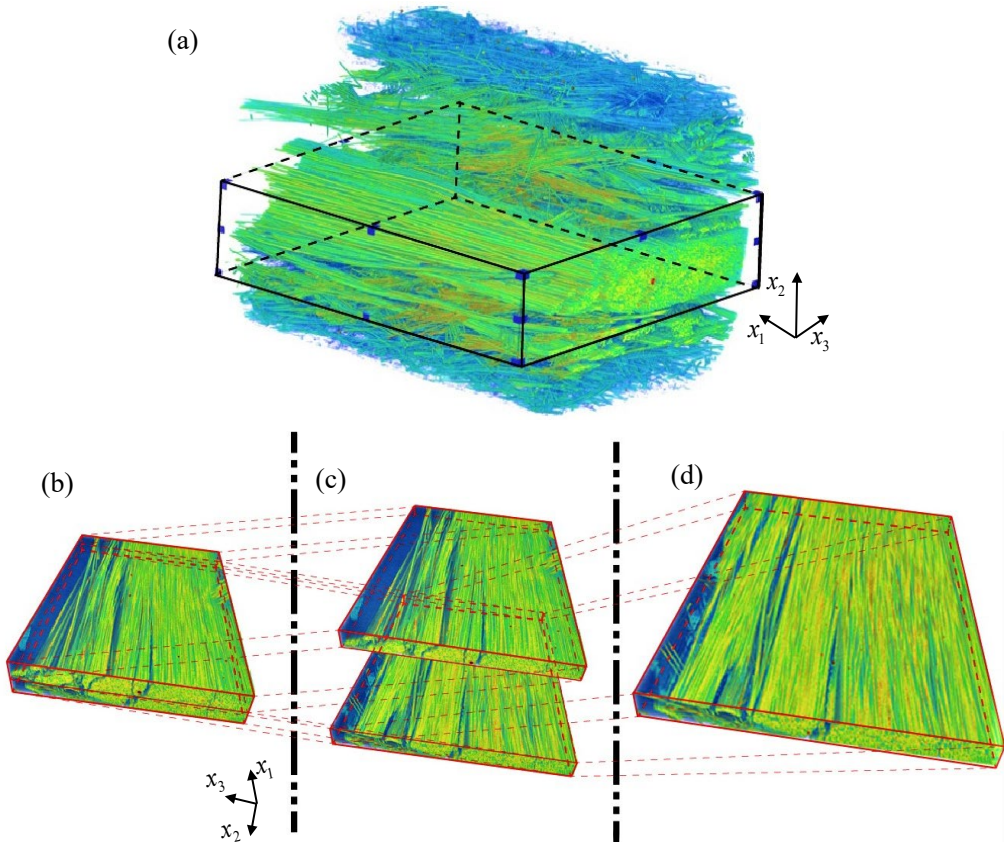

Fig. 11. Colored micro-CT images: (a) HUWCL, (b) The layer of UD laminae, (c) Segments of the UD laminae layer, and (d) A zoom-in image.

4.3. Microscale damage in the woven layer

Fig. 12(a) shows the 3D microstructure of the woven layer. To capture the internal damage modes in the woven layers and reveal their failure mechanism, five slices along the x_2 axis are labelled as '*m*' to '*q*', and the distances betweem each slices can be found in the figure. To further distinguish the influence of the fracture surfraces on the fibers and the initial voids, the images taken from the vicinities of (Figs. 12(b)-(e)) and the area away from (12(f)-(i)) the fracture surface are discussed respectively. Fig. 12(b) and Fig. 12(d) are the microscale damages at slice '*o*' , and Fig. 12(c) and Fig. 12(e) are the microscale damages at slice '*p*' , respectively, around the fracture sruface. In the woven layer, the loadings are mainly transferred to the fibers and the internal fiber fracture can be easily detected as shown in Figs. 12(b)-(c). Mainwhile, the matrix damage propagation from the initial voids can be clearly seen in Figs. 12(d)-(e). Obvious deformation and failure occur almost simultaneously in the fibers and the matrix. Figs. 12(f)-(g) are the microscale morphologies of slice '*m*'. Figs. 12(h)-(i) are, respecitvely, the microscale morphology at slices '*n*' and '*q*'. From the slice images shown in Figs. 12(f)-(i), it can be seen that the farcture is unlikely to cause damage intiated from the exsiting voids that are away from the fracture surface. Also the fibers and the matrix in the region are virtually intact.

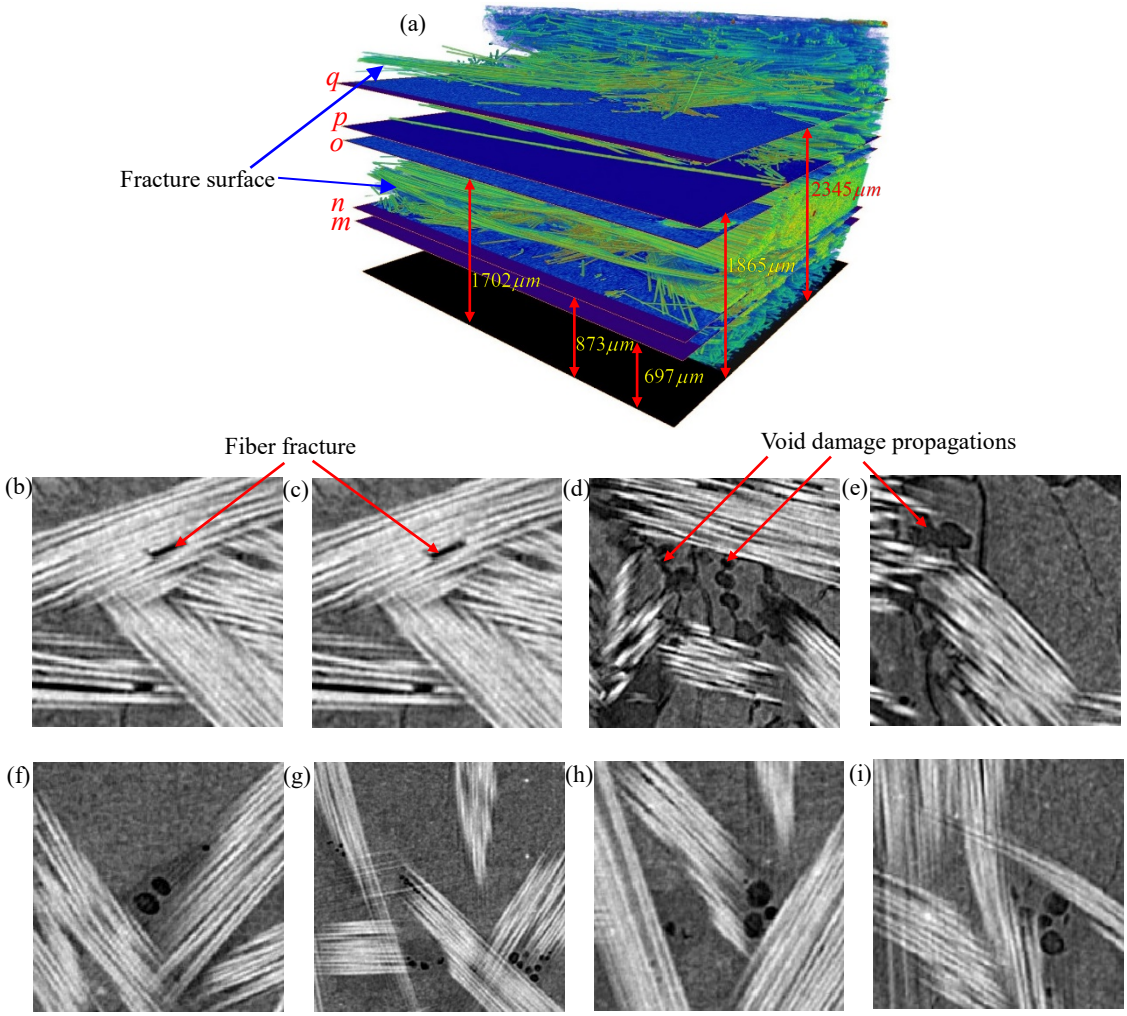

Fig. 12. Sliced images extracted from the woven layer along the thickness direction

5. Interfacial property tests by SEM

Although the micro-CT images show high quality 3D visualization of the formation of transverse cracks and their interaction with delamination, they provide little information on the fiber/matrix debonding at sub-microscale due to its limited spatial resolution. Thus a scanning electron microscope (SEM), TESCAN MAIA3, was further employed to study the fiber-matrix interfacial properties in the UD laminae and the woven layer. Before testing, the specimen was coated with gold by a low vacuum sputtering. A 10-kilovolt voltage was applied on the fractured specimen to acquire magnified images with a desired accuracy.

5.1. Longitudinal load

Fig. 13(a) shows the microscopic morphology of the fractured specimen after being loaded in the longitudinal direction. Some fibers pulled out from the matrix materials can be seen in the woven layer. Fig. 13(b) is a zoomed-in image to further observe the interfacial property between the fibers and the matrix materials. Good interfacial bonding can be found due to the abundant resin matrix adhering to the fiber surfaces. Fig. 13(c) is a zoomed-in image of fiber pull-out from the matrix in the UD laminae layer. The residual matrix material adhering to the fibers also demonstrate a good interfacial boding. Fig. 13(d) is an image to further observe the fiber fracture property. The uneven cross-sections of the fibers suggest that ductile fractures have occurred in the fibers, and the final

failure mode of the UD lamina is mainly attributed to fiber fractures.

By comparing with the resin adhesion on the fiber surfaces shown in Fig. 13(b) and Fig. 13(c), rougher fiber surfaces can be found in the woven layer. It shows that the interfacial bond in the braided fabric layers is better than that of the UD lamina layer. In addition, the continuous fibers and the resin matrix always exhibit linear elastic and viscoplastic properties before the finial failures of the composites occur [32]. From the observations of the rough fiber surfaces of both the UD lamina and the woven layers, it can be concluded that matrix plasticity has a significant effect on the mechanical properties of the HUWCL.

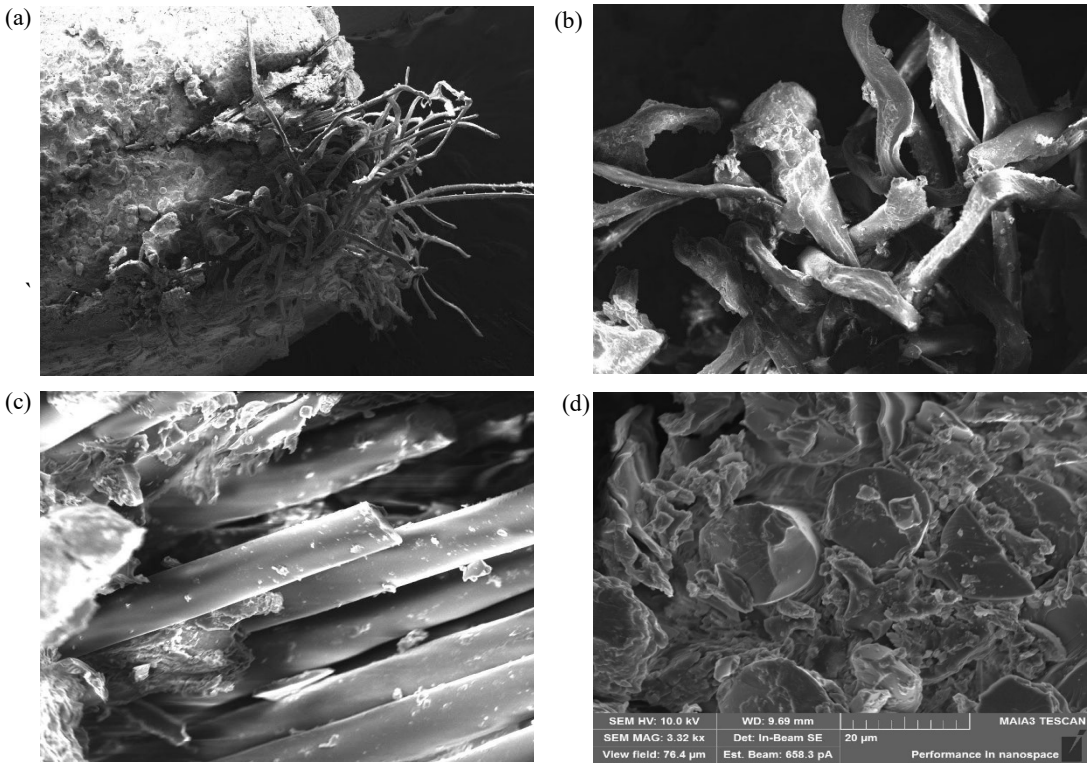

Fig. 13. SEM images of the fracture surface under longitudinal tension: (a) Microscopic morphology of the fracture surface, (b) A zoom-in image of fibers in woven layer, (c) A zoom-in image of fibers in laminae layer, and (d) Fiber cross-section in laminae layer

5.2. Transversal load

Fig. 14(a) shows the morphology of the fractured woven layer under the transversal load. Fig. 14(b) is a zoomed-in image to observe the fiber morphology and the integrity of the interface. In general, the final failure mode of the woven layer is a combination of crimped fiber fractures, matrix cracking. Obvious interfacial debonding around the crimped fibers can be found in the woven layer. While the interfacial bond between the crimped fibers and the matrix materials is strong as excessive residual resins adhering to the fiber surfaces are found, as shown in Fig. 14(b). Moreover, the crimped fibers show ductile fractures due to their unevenly fracture cross-sections. In other words, crimped fibers in woven layers also play an important role in microscale crack propagation.

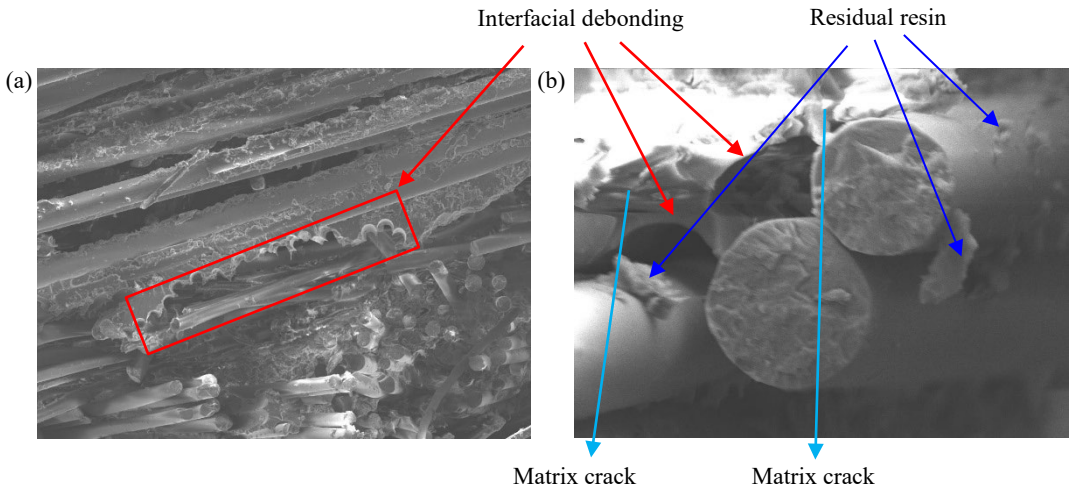

Fig. 14. SEM images of the woven layer under transversal tension: (a) Microscopic morphology of the fracture surface, and (b) A zoom-in image of fibers in woven layer

Matrix cracks exist in the UD laminae is shown in Fig. 15(a). The fibers are fully covered by remnant polyester resin, as seen in Fig. 15(b), showing a very rough surface. This suggests that interfacial bonding between the resin and the fibers is of good quality before applying the transverse loads, and confirms that the transverse cracks are mainly formed by matrix cracking around the fiber/matrix interfaces.

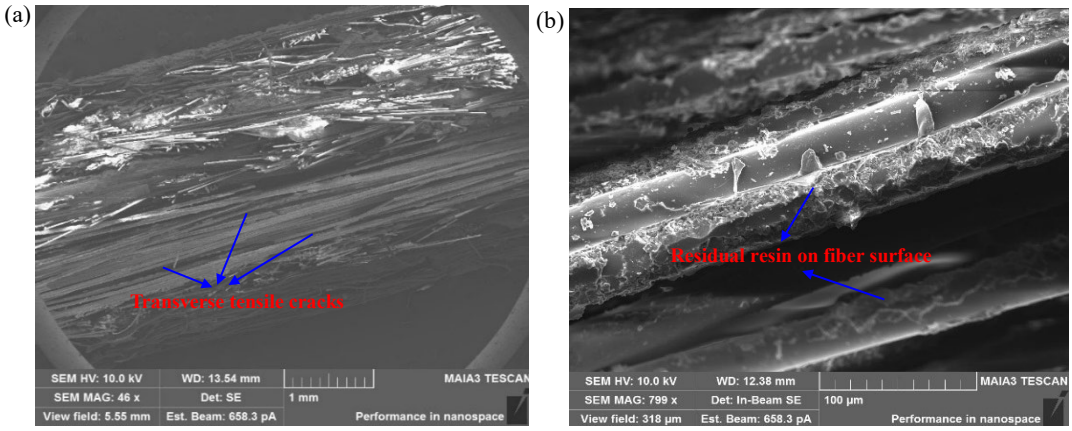

Fig. 15. SEM images of the UD laminae: (a) fractured surface of the specimen and (b) A zoom-in image of fiber/matrix interface

6. Conclusions

In this work, a combined image analysis using micro-CT and SEM was proposed to investigate the microscale structure, local damage and failure of HUWCL. The lay-ups, structural parameters and void ratios of the material are firstly investigated by micro-CT in details. Furthermore, the failure mechanisms of the HUWCL under longitudinal and transverse tensions were investigated by using the experimental visualizations. The conclusions of this study are summarized as below:

(1) In the woven layer, most of elliptical or nearly circular voids were distributed in the vicinity of fiber surfaces, which is likely attributed to insufficient wetting-out during the manufacturing process. However, few initial voids were found in the matrix relatively far away from the fibers.

(2) In the UD layer, elliptical voids, which are mainly in parallel to the fiber direction, are randomly distributed near the fibers.

(3) Under transversal tension, delamination between the woven laminae and the UD laminae is clearly seen. However, no obvious delamination damage was found between the plies of woven laminae. There was a strong correlation between delamination and matrix cracking in the UD lamina.

(4) In general, the final failure mode of the woven layer, when it is subjected to a transversal load, is a collective failure due to crimped fiber fractures, matrix fracture and interfacial debonding. Obvious deformation and failure occur almost simultaneously in the fibers and the matrix near the fracture sruface. In addition, strong interfacial bonding can be found in the UD laminae and the woven layers.

It should be pointed out that the mechanical properties of the HUWCL are dependent on other factors, such as fiber orientations, stacking sequence, fiber distribution, fiber undulation and fiber volume fraction, etc. This paper is restricted to the investigation of the microscale intrinsic properties by experimental tests. It is also a massive challenge to capture the failure sequence for each layer in the HUWCL by experimental tests. This is attributed to the time-consuming immaging process by CT. It is the intention of the authors to develop numerical models informed by the test results presented in this paper to study the influence of the factors mentioned above in the second phase of this research.

Data availability statement

The raw/processed data required to reproduce these findings cannot be shared at this time as the data also forms part of an ongoing study.

CRediT authorship contribution statement

Junjie Ye: Writing-original draft, Conceptualisation. **Heng Cai:** Writing-original draft, Visualization, Data curation. **Lu Liu**: Visualization. **Zhi Zhai:** Visualization, Software. **Amaechi Chiemela Victor:** Visualization, Data curation. **Lei Wan:** Writing-review & editing, Software. **Dongmin Yang:** Visualization, Writing-review & editing, Supervision. **Xuefeng Chen**: Conceptualisation, Supervision. **Jianqiao Ye:** Conceptualisation, Writing-review & editing, Supervision.

Declaration of Competing Interest

The authors declare that they have no known competing financial interests or personal relationships that could have appeared to influence the work reported in this paper.

Acknowledgments

This work was supported by the National Natural Science Foundation of China, China (No. 51675397). The National Natural Science Foundation of Shaanxi Province, China (No. 2018JZ5005). The 111 Project, China (No. B14042). DY would like to thank the financial support from EPSRC for the Zeiss X-ray micro-CT facility and Avizo software under the UKCRIC grant (EP/P017169/1).

References

[1] Cai H, Ye JJ, Wang YW, Saafi M, Huang B, Yang DM, Ye JQ. An effective microscale approach for determining the anisotropy of polymer composites reinforced with randomly distributed short fibers. Compos Struct 2020; 240: 112087.

[2] Xu CB, Yang ZB, Tian SH, Chen XF. Lamb wave inspection for composite laminates using a combined method of sparse reconstruction and delay-and-sum. Compos Struct 2019; 223: 10973.

[3] Ma YQ, Zhao YT, Zhang Y, Wang J, Chen Y, Li KF, Ju LY, Yu Y. Influence of infiltration pressure on the microstructure and properties of 2D-CFRP prepared by the vacuum infiltration hot pressing molding process. Polym 2019; 11(12): 2014.

[4] Xu XW, Ge XL, Liu X, Li LL, Fu K, Dong Y, Meng FB, Si RH, Zhang MH, Two-dimensional M2CO2/MoS2 (M=Ti, Zr and Hf) van der Waals heterostructures for overall water splitting: A density functional theory study. Ceram Int 2020; 46: 13377–13384

[5] Yang DH, Yang ZB, Zhai Z, Chen XF. Homogenization and localization of ratcheting behavior of composite materials and structures with the thermal residual stress effect. Mater 2019; 12(3048):1-20.

[6] Cai H, Ye J.J, Wang YK, Jia F, Hong Y, Tian SH, Chen XF. Matrix failures effect on damage evolution of particle reinforced composites. Mech Adv Mater Struc 2019; DOI: 10.1080/15376494.

[7] Shi PP. Singular integral equation method for 2D fracture analysis of orthotropic solids containing doubly periodic strip-like cracks on rectangular lattice arrays under longitudinal shear loading. Appl Math Model 2020; 77:1460-73.

[8] Ye JJ, Wang YW, Li ZW, Saafi M, Jia F, Huang B, Ye JQ. Failure analysis of fiber-reinforced composites subjected to coupled thermo-mechanical loading. Compos Struct 2020; 235: 111756.

[9] Lal LPJ, Ramesh S, Parasuraman S, Natarajan E, Elamvazuthi I. Compression after impact behaviour and failure analysis of nanosilica-toughened thin Epoxy/GFRP composite laminates. Mater 2019; 12: 1-15.

[10] Ye JJ, Chu CC, Cai H, Hou XN, Shi BQ, Tian SH, Chen XF, Ye JQ. A multi-scale model for studying failure mechanisms of composite wind turbine blades. Compos Struct 2019; 212: 220-9.

[11] Somireddy M, Singh CV, Czekanski A. Mechanical behaviour of 3D printed composite parts with short carbon fiber reinforcements. Eng Fail Analysis 2020; 107: 104232.

[12] Ma YQ, Wang J, Zhao YT, Wei XL, Ju LY, Chen Y. A New Vacuum Pressure Infiltration CFRP Method and Preparation Experimental Study of Composite. Polym 2020; 12(2):419.

[13] Zhang D, Zheng XT, Wu TC. Damage characteristics of open-hole laminated composites subjected to longitudinal loads. Compos Struct 2019; 230: 111474.

[14] Parambil NK, Gururaja S. Micromechanical damage analysis in laminated composites with randomly distributed fibers. J Compos Mater 2016; 50(21): 2911-24.

[15] Hazrati A. Multi-scale analysis of nonlinear fatigue damage behaviour of a quad-core sandwich panel with heterogeneous aluminium sheets. Theor Appl Fract Mec 2019; 99: 79-94.

[16] Sun B, Xu YL, Li ZX. Multi-scale fatigue model and image-based simulation of collective short cracks evolution process. Comp Mater Sci 2016; 17: 24-32.

[17] Rodriguez RQ, Moura LS, Galvis A F. Multi-scale dynamic failure analysis of 3D laminated composites using BEM and MCZM. Eng Anal Bound Elem 2019; 104: 94-106.

[18] Anita C, Marco M. A multi-scale approach for the optimum design of sandwich plates with honeycomb core. Part II: the optimisation strategy. Compos Struct 2014; 118: 677-90.

[19] Ye JJ, Chu CC, Cai H, Wang YK, Qiao XJ, Zhai Z, Chen XF. A multi-scale modeling scheme for damage analysis of composite structures based on the High-Fidelity Generalized Method of Cells. Compos Struct 2018; 206: 42-53.

[20] Boddeti N, Rosen DW, Maute K, Dunn ML. Multiscale optimal design and fabrication of laminated composites. Compos Struct 2019; 228: 111366.

[21] Qiao Y, Deleo AA, Salviato M. A Study on the Multi-axial Fatigue Failure Behavior of Notched Composite Laminates. University of Washington. USA. 2019.

[22] Nguyen NQ, Mehdikhani M, Straumit I, Gorbatikh L, Lessard L, Lomov SV. Micro-CT measurement of fiber misalignment: Application to carbon/epoxy laminates manufactured in autoclave and by vacuum assisted resin transfer moulding. Compos Part A-Appl S 2018; 10: 14-23.

[23] Abrate S. Impact on composite structures. Cambridge University Press; 1998.

[24] Liu HB, Falzon BG, Dear JP. An experimental and numerical study on the crush behaviour of hybrid unidirectional/woven carbon-fiber reinforced composite laminates. Int J Mech Sci 2019; 164: 105160.

[25] Liu HB, Falzon BG, Tan W. Predicting the Compression-After-Impact (CAI) strength of damage-tolerant hybrid unidirectional/woven carbon-fiber reinforced composite laminates. Compos Part A-Appl S 2018; 105: 189-202.

[26] Moleiro F. Carrera E, Li G, Cinefra M, Reddy JN. Hygro-thermo-mechanical modelling of multilayered plates: hybrid composite laminates, fiber metal laminates and sandwich plates. Compos Part B-Eng 2019; 177: 107388.

[27] Gupta A, Ghosh A. Isogeometric static and dynamic analysis of laminated and sandwich composite plates using nonpolynomial shear deformation theory. Compos Part B-Eng 2019; 176: 107295.

[28] Mahmoud B, Manseri L, Rogania A, Navarroa P, Marguet S, Ferrero JF, Tawk I. Experimental and numerical study of the damage mechanisms in hybrid unidirectional/woven composites under impact loading. Compos Struct 2019; 209: 606-15.

[29] Gorzelanczyk T, Pachnicz M, Rozanski A, Schabowicz K. Multi-scale structural assessment of cellulose fibers cement boards subjected to high temperature treatment. Mater 2019; 12(15): 2449.

[30] Lua X, Jin YX. Structure and properties of nylon 12/SiC nanocomposites. Mater Res Exp 2019; 6(6): 065045.
[31] Mangan A P, Whitaker R T. Partitioning 3D surface meshes using watershed segmentation. IEEE T Vis Comput Gr 1999; 5(4): 308-321.
[32] Zhai Z. Multiscale modeling based on generalized cell of method and its application in composite structural health monitoring. Xi'an Jiaotong University, 2014.